

REPORT DOCUMENTATION PAGE

Form Approved OMB NO. 0704-0188

The public reporting burden for this collection of information is estimated to average 1 hour per response, including the time for reviewing instructions, searching existing data sources, gathering and maintaining the data needed, and completing and reviewing the collection of information. Send comments regarding this burden estimate or any other aspect of this collection of information, including suggestions for reducing this burden, to Washington Headquarters Services, Directorate for Information Operations and Reports, 1215 Jefferson Davis Highway, Suite 1204, Arlington VA, 22202-4302. Respondents should be aware that notwithstanding any other provision of law, no person shall be subject to any penalty for failing to comply with a collection of information if it does not display a currently valid OMB control number.

PLEASE DO NOT RETURN YOUR FORM TO THE ABOVE ADDRESS.

1. REPORT DATE (DD-MM-YYYY) 12-06-2008	2. REPORT TYPE Technical Report	3. DATES COVERED (From - To) 1-Nov-2006 - 31-Jul-2007		
4. TITLE AND SUBTITLE Subwavelength Imaging		5a. CONTRACT NUMBER W911NF-07-1-0019		
		5b. GRANT NUMBER		
		5c. PROGRAM ELEMENT NUMBER 611102		
6. AUTHORS Huikan Liu, Shivanand, and Alon Ludwig, Kevin J. Webb		5d. PROJECT NUMBER		
		5e. TASK NUMBER		
		5f. WORK UNIT NUMBER		
7. PERFORMING ORGANIZATION NAMES AND ADDRESSES Purdue University Sponsored Programs Services Young Hall, 302 Wood Street West Lafayette, IN 47907 -2108		8. PERFORMING ORGANIZATION REPORT NUMBER		
9. SPONSORING/MONITORING AGENCY NAME(S) AND ADDRESS(ES) U.S. Army Research Office P.O. Box 12211 Research Triangle Park, NC 27709-2211		10. SPONSOR/MONITOR'S ACRONYM(S) ARO		
		11. SPONSOR/MONITOR'S REPORT NUMBER(S) 51886-PH.1		
12. DISTRIBUTION AVAILABILITY STATEMENT Approved for Public Release; Distribution Unlimited				
13. SUPPLEMENTARY NOTES The views, opinions and/or findings contained in this report are those of the author(s) and should not be construed as an official Department of the Army position, policy or decision, unless so designated by other documentation.				
14. ABSTRACT The imaging properties of a uniaxial anisotropic slab lens, where the dielectric tensor components are of opposite sign, are studied as a function of the structure parameters. While hypothetical parameters yield various levels of performance, a design principle to achieve good sub-wavelength resolution is suggested. The anisotropy can be implemented with a metal-insulator stack.				
15. SUBJECT TERMS Imaging, subwavelength, nanophotonics				
16. SECURITY CLASSIFICATION OF: a. REPORT U		17. LIMITATION OF ABSTRACT b. ABSTRACT U c. THIS PAGE U SAR	15. NUMBER OF PAGES	19a. NAME OF RESPONSIBLE PERSON Kevin Webb
				19b. TELEPHONE NUMBER 765-494-3373

Report Title

Subwavelength Imaging

ABSTRACT

The imaging properties of a uniaxial anisotropic slab lens, where the dielectric tensor components are of opposite sign, are studied as a function of the structure parameters. While hypothetical parameters yield various levels of performance, a design principle to achieve good sub-wavelength resolution is suggested. The anisotropy can be implemented with a metal-insulator stack.

The influence of material and thickness on the subwavelength imaging performance of a negative dielectric constant slab is studied. Resonance in the plane wave transfer function produces a high spatial frequency ripple that could be useful in fabricating periodic structures. A cost function based on the plane wave transfer function provides a useful metric to evaluate the planar slab lens performance, and using this, the optimal slab dielectric constant can be determined.

Prospects for a lossless negative dielectric constant material for optical devices are studied. Simulations show that with sufficient gain, a mixture of two semiconductor quantum dots can produce an isotropic effective dielectric constant that is lossless and negative. Over length scales where homogenization is meaningful, this permits a small-scale optical mode volume and lossless waveguides, major goals in the field of nanophotonics.

We show quantitatively the influence of dipole density on the resolving capability of a negative refractive index slab. A numerical solution for scatter with a model that represents a locally periodic array of electric and magnetic dipoles provides a means for evaluating the influence of periodicity. A Fourier transform of the spatial field solution gives access to the plane wave transfer function in relation to the degree of granularity. Throughout, a quasi-static homogenization procedure is used to ensure that correctly matched effective medium parameters are achieved. The results provide a measure of the fabrication technology necessary to achieve substantially subwavelength resolution.

We suggest, based on the principle of causality, and for a material exhibiting adjacent absorptive and gain resonances, that there can be an intervening frequency where perfect imaging is in concept possible. At this frequency, both the dielectric constant and the permeability are negative, leading to a negative refractive index, and there is no loss. In such a material exhibiting a double resonance, the gain must be at the higher frequency. Through appropriate tuning of the refractive index, all propagating and evanescent fields from the object could then in principle be reconstructed at the image plane, subject to practical implementation limits.

The work reported resulted in the production of five journal papers.

Subwavelength Imaging

Kevin J. Webb, Huikan Liu, Shivanand, and Alon Ludwig
School of Electrical and Computer Engineering, Purdue University
465 Northwestern Ave, West Lafayette, IN 47907-2314
webb@purdue.edu

Abstract

The imaging properties of a uniaxial anisotropic slab lens, where the dielectric tensor components are of opposite sign, are studied as a function of the structure parameters. While hypothetical parameters yield various levels of performance, a design principle to achieve good sub-wavelength resolution is suggested. The anisotropy can be implemented with a metal-insulator stack.

The influence of material and thickness on the subwavelength imaging performance of a negative dielectric constant slab is studied. Resonance in the plane wave transfer function produces a high spatial frequency ripple that could be useful in fabricating periodic structures. A cost function based on the plane wave transfer function provides a useful metric to evaluate the planar slab lens performance, and using this, the optimal slab dielectric constant can be determined.

Prospects for a lossless negative dielectric constant material for optical devices are studied. Simulations show that with sufficient gain, a mixture of two semiconductor quantum dots can produce an isotropic effective dielectric constant that is lossless and negative. Over length scales where homogenization is meaningful, this permits a small-scale optical mode volume and lossless waveguides, major goals in the field of nanophotonics.

We show quantitatively the influence of dipole density on the resolving capability of a negative refractive index slab. A numerical solution for scatter with a model that represents a locally periodic array of electric and magnetic dipoles provides a means for evaluating the influence of periodicity. A Fourier transform of the spatial field solution gives access to the plane wave transfer function in relation to the degree of granularity. Throughout, a quasi-static homogenization procedure is used to ensure that correctly matched effective medium parameters are achieved. The results provide a measure of the fabrication technology necessary to achieve substantially subwavelength resolution.

We suggest, based on the principle of causality, and for a material exhibiting adjacent absorptive and gain resonances, that there can be an intervening frequency where perfect imaging is in concept possible. At this frequency, both the dielectric constant and the permeability are negative, leading to a negative refractive index, and there is no loss. In such a material exhibiting a double resonance, the gain must be at the higher frequency. Through appropriate tuning of the refractive index, all propagating and evanescent fields from the object could then in principle be reconstructed at the image plane, subject to practical implementation limits.

The work reported resulted in the production of five journal papers.

1 Summary of project

Traditional imaging systems or lenses operate in the far field and have spatial resolution limited by the wavelength. This restriction on the spot size occurs because of the diminishing evanescent fields with increasing distance from the object, and the image is formed in the far-field. This means that imaging systems where resolution is important, such as in optical lithography for semiconductor devices, must use smaller wavelengths in order to achieve finer features. This limitation can be circumvented by spatially limiting the detection area, as is done in a near-field scanning optical microscope (NSOM). While the NSOM is a powerful tool, it is not useful for many applications (lithography, for example), and the tip must be mechanically moved, which can be difficult and slow.

If it were possible to achieve subwavelength image resolution without use of a small aperture then the impact on optics would be enormous. Imaging elements could be very small, the resolution of optical microscopes could be improved, optical interconnects in and between chips could be practical, optical storage devices could contain much more data, optical signal processing would be revolutionized, and optical lithography could be used to achieve much small chip feature sizes.

Much of the excitement about negative index materials relates to two possible characteristics, negative refraction, which allows planar lenses and, more importantly, with small loss, growth of evanescent

fields, which can facilitate subwavelength imaging. As there are no known materials having both negative permittivity and permeability, a requirement for negative index, use of metamaterials has been explored. The difficulty with achieving a true negative index material that provides subwavelength resolution is the need for both high dipole density and low loss, and the need for a magnetic response at the wavelength. As we have shown, any loss moves operation to the near field and limits the resolution [1, 2].

Use of a thin metal layer “lens” and the correct polarization can produce subwavelength features in the near field. We have found that use of a metal film stack can provide significant improvement in the evanescent field performance, i.e., much smaller spot size [3]. We have done a preliminary analysis of a metamaterial film structure that will provide the best resolution of any imaging device that does not have limited spatial support, such as could be defined by a small aperture. Our plan is to study various structures that have potential for subwavelength imaging.

2 Introduction

Conventional optics suffers from the diffraction limit because only the propagating components of the plane wave spectrum are available. As a consequence, the spot size is limited to about one wavelength. There is therefore a link between memory density and wavelength, for example. Information about the subwavelength features of the object are carried by the evanescent waves, which decay exponentially. Subwavelength imaging is of fundamental importance in fields as varied as semiconductor device lithography, optical memory and microscopy. The subwavelength information is conveyed in the evanescent (non-propagating) portion of the plane wave spectrum. A negative refractive index slab can act as a lens because of negative refraction, and of particular interest, can amplify the evanescent fields and produce images with subwavelength features [4, 5, 1, 2]. The primary features which negative index materials (NIMs) offer are: negative refraction, evanescent field growth, leading to the prospect of subwavelength imaging, and dispersion. These characteristics, individually and collectively, are important for imaging and a variety of other optical signal processing applications, in which an incident field (or set of fields) is transformed in some manner at the output (such as to a subwavelength spot). While building negative index materials at optical wavelengths will be very challenging, achieving low-loss structures which perform the aforementioned operations is possible now.

We have shown that a layered metal-insulator stack has the capability of subwavelength imaging [6]. It works because the effective dielectric constant is anisotropic and hence the structure converts evanescent fields from the source (the object) to propagating wave the multi-layer stack. In this way, information about the evanescent fields from the source can be conveyed to the image plane.

3 Results

3.1 Sub-wavelength imaging opportunities with planar uniaxial anisotropic lenses

The imaging properties of a uniaxial anisotropic slab lens, where the dielectric tensor components are of opposite sign, are studied as a function of the structure parameters. While hypothetical parameters yield various levels of performance, a design principle to achieve good sub-wavelength resolution is suggested. The anisotropy can be implemented with a metal-insulator stack.

Referring to Fig. 1, we assume dielectric constants $\epsilon_x = \epsilon'_x + j\epsilon''_x$ and $\epsilon_z = \epsilon'_z + j\epsilon''_z$, with time dependence $\exp(j\omega t)$. For the TM wave (extraordinary wave with H_y), the dispersion relation is $k_x^2\epsilon_z^{-1} + k_z^2\epsilon_x^{-1} = k_0^2$ (and in free space, $k_x^2 + k_{z0}^2 = k_0^2$). In the absence of loss, if $\epsilon_x > 0$ and $\epsilon_z < 0$, the structure couples the incident plane wave fields (propagating or evanescent) to propagating waves. As a result, higher spatial frequency Fourier components with $k_x > k_0$ are available at the output plane and hence for subwavelength imaging [7, 8].

The transmission coefficient for H_y is given by

$$T(k_x) = \frac{1}{\cos(k_z d) + \frac{j}{2}(\frac{Z_s}{Z_0} + \frac{Z_0}{Z_s})\sin(k_z d)}, \quad (1)$$

where $Z_s = k_z/\omega\epsilon_x\epsilon_0$ and $Z_0 = k_{z0}/\omega\epsilon_0$ denote the characteristic impedance of the slab and the surrounding medium, respectively, with ϵ_0 the free space permittivity.

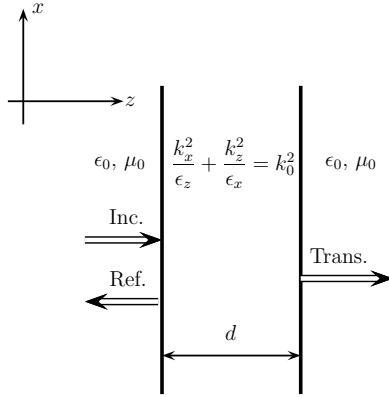
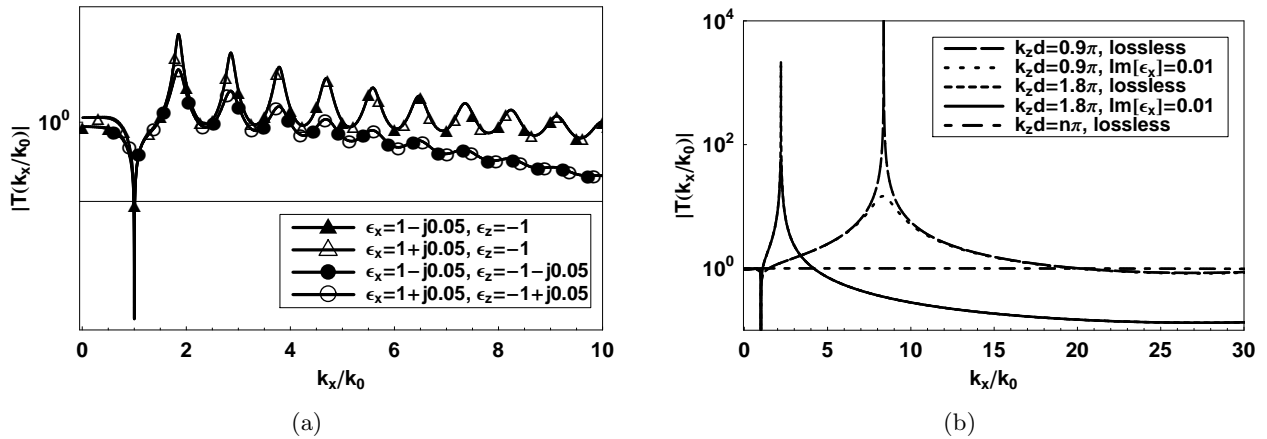


Figure 1: Anisotropic slab structure.

Figure 2: Transmission spectrum for (a) lossy or optically amplifying media, and (b) the $\epsilon_z \rightarrow \infty$ lens. The parameters are $\lambda = 700\text{nm}$, $d = 400\text{nm}$.

For the deep evanescent spectrum, the magnitude of transmission coefficient remains unchanged if ϵ_x'' and ϵ_z'' change signs simultaneously. While optical gain could offset the adverse impact of loss [9], overcompensation of loss will detract from the resolution. Figure 2(a) shows an example where $\epsilon_x = 1 - j0.05$, $\epsilon_z = -1 - j0.05$, and $\epsilon_x = 1 + j0.05$, $\epsilon_z = -1 + j0.05$, have essentially identical $|T(k_x/k_0)|$ throughout the evanescent spectrum ($k_x/k_0 > 1$).

Subject to low loss, tuning $\epsilon_x \epsilon_z$ close to -1 , and making ϵ_x less positive and ϵ_z more negative should improve the resolution, and some loss to dampen singularities are beneficial. In Fig. 3(a), with ϵ_x/ϵ_z fixed, the best resolution is achieved, as anticipated, with $\epsilon_x = 0.01 - j0.01$ and $\epsilon_z = -100$, for which $\epsilon_x \epsilon_z$ is closest to -1 . Figure 3(b) shows that, with $\epsilon_x \epsilon_z$ constant, the lens with the lowest value of $|\epsilon_x/\epsilon_z|$ (corresponding to $\epsilon_x = 0.01 - j0.01$) gives the best resolution.

With $\epsilon_z \rightarrow \infty$ and $\epsilon_x \rightarrow 0$, a pole of the transfer function given by

$$\frac{k_x}{k_0} = \sqrt{1 + \left(\frac{k_0 d}{2}\right)^2}, \quad (2)$$

occurs, implying that the pole is uniquely determined by the slab thickness d at a fixed frequency. Although $\epsilon_z \rightarrow \infty$ and $\epsilon_x \rightarrow 0$ do not make a perfect lens because of the transmission singularity, these limits together with small slab absorption may hold promise for nearly perfect imaging. The underlying physical mechanism relies on the fact that $\epsilon_z \rightarrow \infty$ reduces sensitivity to the transverse wave vector k_x , or in terms of the “preferred direction” [10], $\epsilon_z \rightarrow \infty$ eliminates the divergence of wave components by enforcing the “preferred direction” parallel to the optical axis, and $\epsilon_x \rightarrow 0$ ensures the slab is electrically thin, regardless of its physical thickness.

If

$$d = n \frac{\lambda}{2} \quad \text{or} \quad k_z d = \sqrt{\epsilon_x} k_0 d = n\pi, \quad n = 1, 2, \dots \quad (3)$$

the amplitude of the transfer function becomes unity, and under this resonant condition, the lens is perfect. More specifically, $k_z d = 2n\pi$ results in a “zero-phase shift” perfect lens, whereas $k_z d = (2n+1)\pi$ leads to a “ π -phase shift” perfect lens. Note that $\epsilon_z \rightarrow \infty$ fulfills the condition of the canalization regime [11, 12, 13]. A small deviation of $\sqrt{\epsilon_x} k_0 d$ from $n\pi$ introduces a pole, thereby compromising the system resolution. Figure 2(b) shows the transmission coefficient magnitude for a perfect lens and lenses operating near this condition, where singularities occur. In Fig. 3(c), lenses operating in the multiple half-wavelength regime exhibit similar resolution to the electrically thin lenses, whereas in Fig. 3(d), a small deviation from the perfect condition, say, a variation of thickness d leading to $\text{Re}(k_z d) = 0.95\pi$, significantly impacts the field profile and in turn the resolution, relative to the electrically thin lens. Our comparison between the two types of lenses, as given in Figs. 3(c) and 3(d), suggests that the electrically thin lens may be superior to the resonant slab lens because $\epsilon_x \rightarrow 0$ removes the strict requirement on the physical thickness. The resonant perfect lenses in Fig. 3(c) do not restore the source completely in the image plane because of the mask geometry, but the field on the left interface of the anisotropic slab is replicated on the right surface.

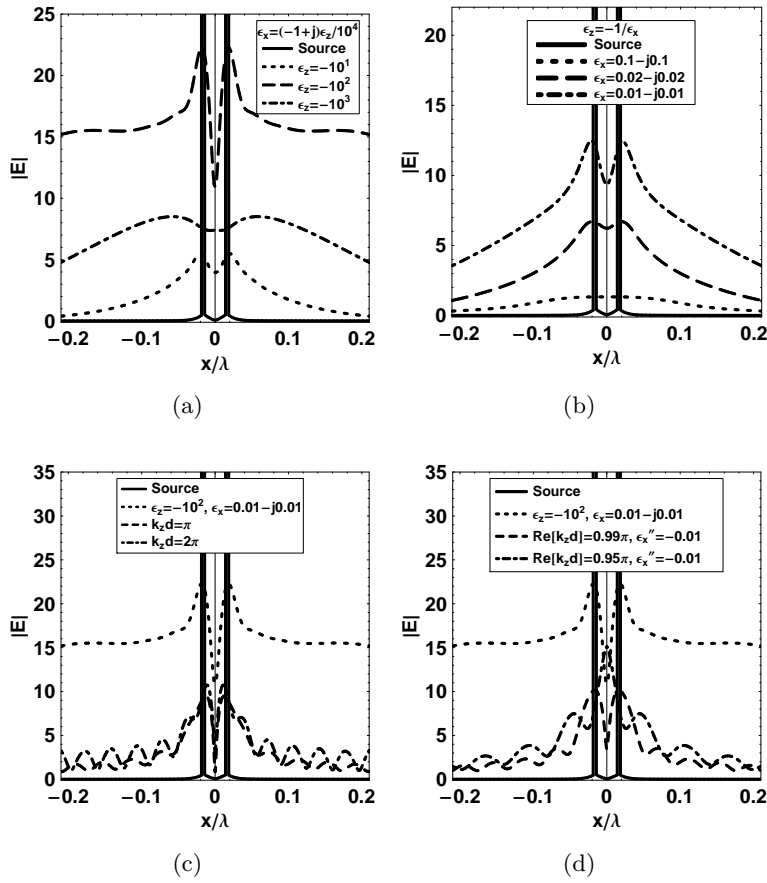


Figure 3: Double-slit resolution of an anisotropic slab lens, based on finite element simulations, with various material parameters: (a) ϵ_x/ϵ_z is constant; (b) $\epsilon_x\epsilon_z$ is constant; (c) $\epsilon_x \rightarrow 0$, $\epsilon_z \rightarrow \infty$ and the perfect lens; (d) $\epsilon_x \rightarrow 0$, $\epsilon_z \rightarrow \infty$ and deviation from the perfect lens. The parameters are: $\lambda = 700\text{nm}$, $d = 400\text{nm}$.

3.2 Imaging performance of an isotropic negative dielectric constant slab

We explore the near-field imaging properties of a single slab of material with isotropic $\epsilon = \epsilon' + j\epsilon''$, with $\epsilon' < 0$. This condition is satisfied, for example, by metals at optical frequencies. It is also possible to synthesize materials that have these properties, such as mixtures of metals and dielectrics,

and fabrication can be relatively straight forward. While this system has received considerable recent attention, we are motivated to understand what resolution range is accessible, how to measure resolution, and potential applications.

We consider a TM field and a free space background. For an isotropic slab with dielectric constant ϵ , the dispersion relation is $k_x^2 + k_z^2 = \epsilon k_0^2$, where in free space $k_0^2 = \omega^2/c^2$, with c the velocity. Following the $\exp(j\omega t)$ time convention, the transmission coefficient is

$$T(k_x) = \frac{(1-r^2)\exp(-jk_zd)}{1-r^2\exp(-j2k_zd)}, \quad (4)$$

where r is the reflection coefficient and d is the thickness of the slab [6]. Singularities in eq(4) occur when $r^2 = \exp(j2k_zd)$. It is this property of the transmission coefficient approaching infinity that we want to exploit for achieving an improved image resolution. Also, in the off-resonance conditions, we have $T(k_x) \approx (1-r^2)\exp(-k_xd)$ for large k_x and real ϵ , making the slab thickness a dominant parameter in imaging performance.

A perfect lens has $T(k_x) = 1$ and, generally, the resolution can be expected to improve as $T(k_x)$ increases deep in the evanescent (free space) plane wave spectrum. This occurs for decreasing slab thickness d , and practical considerations drive this standoff distance between the object and image planes. The singularities, which dampen with loss, are undesirable in an imaging application.

Within the object spatial support, the incident field is defined by $H_y = 1$, i.e., the incident field is defined by $H_y(x) = p(x - a, w)$, where $p(x - a, w)$ is a unit amplitude pulse centered at $x = a$ and of width w . A plane wave expansion of this excitation was used to solve for H_y in each region, and \mathbf{E} was determined from an inverse Fourier transform of the plane-wave spectrum for H_y multiplied by the impedance.

Singularities in $T(k_x)$ produce dominant image plane effects corresponding to those spatial frequencies. The dominant influence of the singularity causes a ripple at this spatial frequency. Through this mechanism, by control of the complex dielectric constant, it is in concept possible to generate a periodic spatial ripple with arbitrarily high frequency. This could be useful in lithography for very dense (relative to the illuminating wavelength) periodic systems (photonic crystals). How practical this is rests on how easily the dielectric constant can be controlled, in particular, the imaginary part.

Passive materials will have some loss, and we explore the influence of ϵ'' in Fig. 4. Fig. 4(a) shows the magnitude of the transmission spectrum obtained for a $0.1 \mu\text{m}$ thick slab having $\epsilon' = -1.01$. Clearly, the loss suppresses the singularities. With an object $H_y(x) = p(x, 0.01\lambda)$ and a $d = 0.1 \mu\text{m}$ thick slab having $\epsilon' = -1.01$ and various ϵ'' , we obtain the electric field images of Fig. 4(b). The full width, half maximum (FWHM) of the images is: 0.265λ for $\epsilon = -1.01 - j0.01$; 0.235λ for $\epsilon = -1.01 - j0.02$; 0.255λ for $\epsilon = -1.01 - j0.05$; and 0.295λ for $\epsilon = -1.01 - j0.1$. As a reference, the FWHM after propagation over $0.1 \mu\text{m}$ in free space is found to be 0.415λ . It is clear from this example that the best performance is not obtained when the loss is minimum. This leads to the need to optimize the lens parameters for the best results. A well chosen cost function can be used to optimize the parameters of the transfer function.

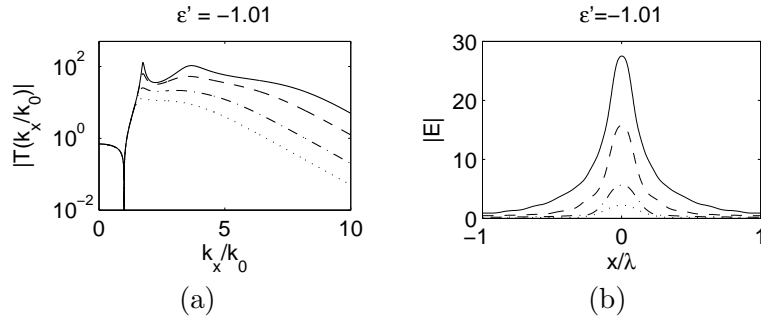


Figure 4: (a) The magnitude of the transmission coefficient for a $0.1 \mu\text{m}$ thick slab having various $\epsilon = -1.01 - j\epsilon''$. (b) $|\mathbf{E}|$. The line types correspond to: $\epsilon'' = 0.01$ (solid) $\epsilon'' = 0.02$ (dashed) $\epsilon'' = 0.05$ (dash-dotted) $\epsilon'' = 0.1$ (dotted) The free space wavelength is $\lambda = 700 \text{ nm}$.

We choose the function

$$C(\epsilon, d) = \int \frac{|\mathbb{F}^{-1}(T(k_x/k_0))|}{\max[|\mathbb{F}^{-1}(T(k_x/k_0))|]} dx, \quad (5)$$

where \mathbb{F}^{-1} is the inverse Fourier transform. Equation (5) takes into consideration both the magnitude as well as the phase of the transmission coefficient and has been used for our results. For a perfect lens, $C = 0$. With $\lambda = 700$ nm, we searched for the minimum $C(\epsilon, d)$ for a series of d/λ using a step size of $\delta d/\lambda \approx 0.071$. We found the optimum ϵ at each d/λ , based on the minimum of (5), and the result is given in Fig. 5(a). The best resolution is when ϵ' is slightly less than -1 . Also, ϵ'' has been optimized for minimum cost. Notice that the optimal ϵ'' for $d/\lambda < 1$ is small, but non-zero. Fig. 5(b) shows the FWHM of $|\mathbf{E}|$ in the image plane for the optimal ϵ shown in Fig. 5(a). An object of width 0.01λ was used. As the slab thickness increases, the lens performance deteriorates, but it is still substantially better than the free space case, given by the $\epsilon = 1$ curve. The FWHM is subwavelength only for $d/\lambda < 1$, making this the useful regime. For thicker lenses, a larger loss (ϵ'') gives the minimum cost and hence smaller FWHM. This loss produces a propagating component, clearly important with increasing thickness. However, this large loss significantly reduces the amplitude of the electric field in the image plane. Our studies thus far suggest that (5) is a useful metric.

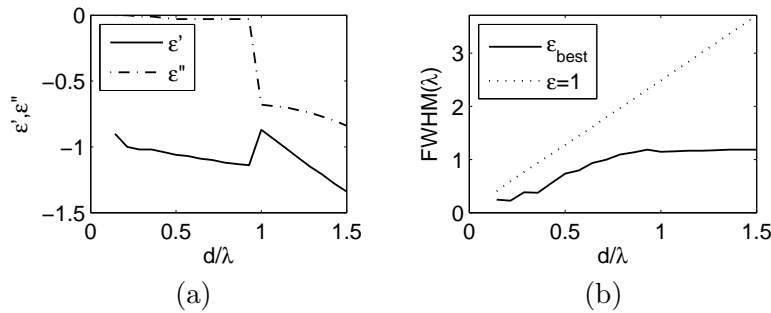


Figure 5: (a) Optimal ϵ obtained from the cost function (5), for various slab thickness d . (b) Optimal FWHM for $|\mathbf{E}|$ as a function of d . The d/λ scale should be interpreted as various d with $\lambda = 700$ nm. The object in (b) has width 0.01λ .

3.3 Anisotropic route to optical circuits

By exploiting the optical scattering properties of a single slab with a uniaxial dielectric tensor having $\epsilon_k = \epsilon'_k + i\epsilon''_k$ ($k = x, y, z$) (as in Fig. 6), we find that for the transverse-magnetic polarization incident light the slab can play a role of (a) a distributed transmission line (Fig. 6(a)); (b) a lumped series inductor (Fig. 6(b)); and (c) a lumped shunt capacitor (Fig. 6(c)). In contrast to the realization of circuit nanoelements in the optical domain using nanoparticles [14, 15], the present approach to optical circuits bears two compelling virtues: frequency-independence, and high insensitivity to the angle of incidence or the orientation of the slab relative to the incident wave. Since the circuit parameters are uniquely determined by the dimensions and material parameters of the slab (Fig. 6), the optical circuit elements can effectively operate over a wide range of frequencies and incidence angles, thereby allowing us to export and transplant various microwave and RF circuit functional designs to the infra-red and visible frequency regime more conveniently. The slab is assumed infinitely wide in the derivation, but practically a large aspect ratio (width to length) or large local curvature (relative to the wavelength) suffices the circuit approximation. Finally, we note that the desired anisotropy can be achieved with a metal-insulator stack or wire media [16, 17, 8, 18].

An optical low-pass filter structure is depicted in Fig. 7(a). We used both Chebyshev (equal ripple) and Butterworth (maximally flat) polynomials to determine the L-C values having a normalized cut-off frequency $f/f_0 = 1$ [19]. Fig. 7(b) shows the magnitude of the transfer function for H_y for both normal ($k_x = 0$) and oblique ($k_x = 0.8k_0$) incidence. The frequency roll-off for $f/f_0 > 1$ is dictated by the number of sections. Fig. 7(c) shows the isotropic layer solution, which is quite similar at normal incidence, but deteriorates rapidly as the angle of incidence is moved off normal, illustrating the robustness to the incident angle of transmission property for anisotropic low-pass filters compared to the isotropic case.

Impedance matching/transforming structures provide a means to substantially reduce the scattering cross-section. Fig. 8(a) illustrates a bilayer $L - C$ section that can eliminate reflections from a semi-infinite Ag layer. Fig. 8(b) shows the TM (H_y) reflection coefficient magnitude as a function of incidence angle (k_x/k_0) for bilayer matching to Ag. The two types of capacitors ($\epsilon_z \rightarrow \infty$ and $\epsilon_z = 1$) are shown, and the performance with the $\epsilon_z = 1$ is slightly better. For comparison, Fig. 8(b) shows an isotropic

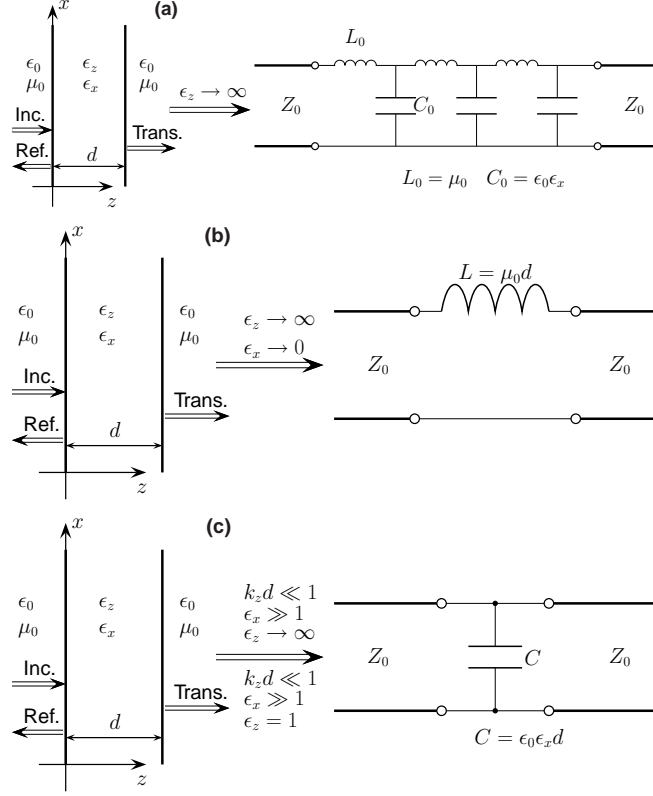


Figure 6: (a) Equivalent transmission line in the optical regime from envisioning an anisotropic slab when $\epsilon_z \rightarrow \infty$. (b) An anisotropic slab with $\epsilon_z \rightarrow \infty$, $\epsilon_x \rightarrow 0$ could play the role of an optical lumped inductor in response to incident TM waves. (c) Equivalent capacitor when $k_z d \ll 1$, $\epsilon_x \gg 1$, $\epsilon_z \rightarrow \infty$ (or $\epsilon_z = 1$).

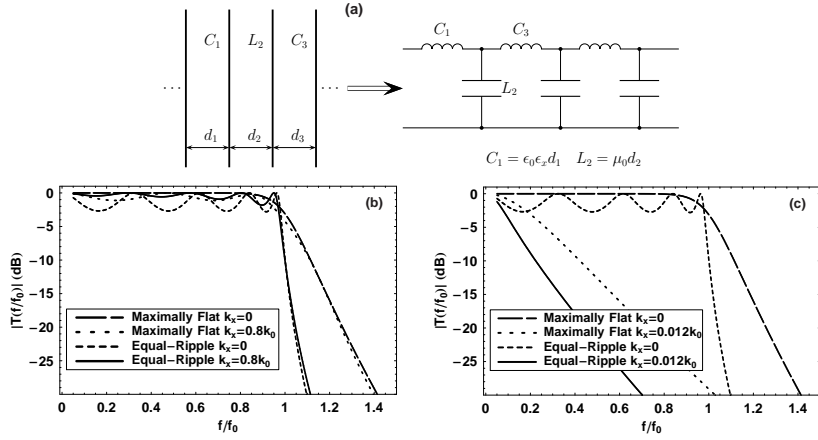


Figure 7: (a) Synthesis of a low-pass filter L-C ladder network. (b) Frequency response of 9-section Chebyshev (equal-ripple, with film thicknesses $l_i (i = 1, \dots, 9) = \{28.1, 308.3, 37.2, 322.6, 37.6, 322.6, 37.2, 308.3, 28.1\}$ nm) and 10-section Butterworth (maximally flat, with thicknesses $l_i (i = 1, \dots, 10) = \{2.5, 360.8, 11.2, 708.0, 15.7, 784.9, 14.2, 561.9, 7.2, 124.3\}$ nm) low-pass filters with normal and oblique incidence. Each anisotropic film assumes $\epsilon_z \rightarrow \infty$, and $\epsilon_x = 50$ for the capacitor and $\epsilon_x = 10^{-3}$ for the inductor. The wavelength corresponding to f_0 is $\lambda_0 = 2500$ nm. (c) Filters with the parameters in (b) and isotropic dielectric constants: $\epsilon = 50$ for C and $\epsilon = 10^{-3}$ for L .

anti-reflection coating, and this shows much greater sensitivity to angle of incidence. Achieving a low reflection for a wide range of incidence angles, because of the anisotropy of the coating, allows substantially reduced object visibility. To illustrate this, Fig. 8(c) shows that scattering cross-section for a 2-D Ag ellipse, with an incident TM wave along the semi-minor axis. Figs. 8(d) and (e) show $|H_y|$ without and with the $L - C$ coating (the wave is incident from the right). The result for a bilayer having $\epsilon_z \rightarrow \infty$ appears superior. The improved anti-reflection properties of the coating could also find

applications in efficient solar energy collectors and other electro-optical devices [20].

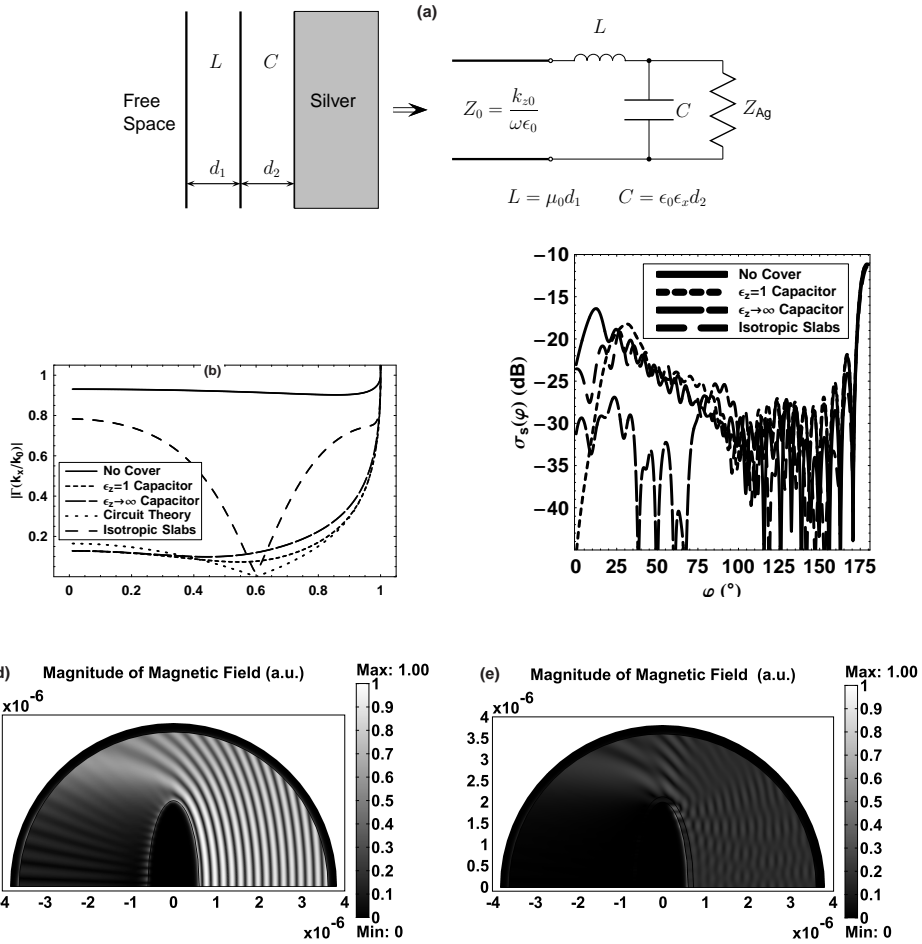


Figure 8: (a) An $L - C$ bilayer anti-reflection coating on Ag. (b) Bilayer TM reflection coefficient. Parameters: $\lambda = 400$ nm, $\epsilon_{Ag} = -3.77 + i0.6747$ [21], $\epsilon_z = 10^3$, $\epsilon_x = 50.0$ for C , $\epsilon_x = 10^{-3}$ for L , $d_1 = 124$ nm, $d_2 = 3.0$ nm. The result for an isotropic quarter-wave transformer ($\epsilon = 3.0$ and length 92.6 nm), on a spacer layer ($\epsilon = 45.4$ and length 14.9 nm) provides a reference. (c) Simulated back-scattering cross section of the scatter with and without the bilayer cover. $|H_y(x, z)|$ for a Ag ellipse under TM wave excitation without (d) and with (e) the bilayer cover.

3.4 Lossless negative dielectric constant optical material based on a semiconductor quantum dot mixture

We show that a metamaterial with a negative dielectric constant at an (optical) frequency where the loss goes to zero, i.e., $\epsilon(\omega_0) = \epsilon'(\omega_0) + i\epsilon''(\omega_0)$ with $\epsilon''(\omega_0) = 0$, can be devised using a semiconductor quantum dot (QD) mixture. This type of metamaterial is of fundamental importance in nanophotonics, where the down-scaling of high density optical components that are based on metal-insulator-metal waveguiding, is limited by the high losses inside the metals [22]. Exchanging the metals by a semiconductor QD mixture with a similar negative dielectric constant but no losses, would allow small waveguide mode volumes and hence high density optical elements and circuits [23, 24].

Resonant states in semiconductors provide a source for negative dielectric constant, provided that the dipole strength and oscillator density is adequate to offset the background. Furthermore, semiconductors offer the prospect of pumping, either optically or electrically, to achieve a gain mechanism that may offset the loss. Previously, a model for a charged QD array has shown a negative real part of the dielectric constant, suggesting isotropic metal-like properties [25].

There is a large body of work describing the scattering of light from QD structures that provide electron-hole (exciton) confinement in three-dimensions (for example, [26, 27, 28, 29, 30, 31, 32, 33, 34]). Models typically employ an effective mass approximation, where the structure is assumed large

relative to the crystal lattice dimension. In the case of a spherical QD under the strong confinement approximation, we assume a simplified model where the wave function can be written as the product of the confined electron and hole functions. This makes it possible to write an analytic solution where the energies of single particles can be summed for the total energy [26, 28]. Assuming also that the spherical potential well has infinite barriers, one can use a quantum mechanical derivation to arrive at the relation

$$\epsilon_{QD} = \epsilon_\infty + \frac{8e^2}{V\epsilon_0 m_e^*} \left[\frac{(2\rho_{gg}^{(0)} - 1)}{\omega_{ex}^2 - \omega^2 - i2\omega\gamma} \right]. \quad (6)$$

where ϵ_∞ is the matched dielectric constant of the background material inside the QD, e is the electron charge, ϵ_0 is the free space permittivity, m_e^* is the effective mass of the electron, ω_{ex} is the resonance angular frequency or the exciton, γ is the phenomenological damping factor, and ω is angular frequency at which the dielectric constant of the QD is calculated. Also in (6), $\rho_{gg}^{(0)}$ is the steady state probability of the quantum mechanical exciton system being in the ground state. Neglecting thermally excited electrons, we have $\rho_{gg}^{(0)} = 1$ for the lossy resonance and $\rho_{gg}^{(0)} = 0$ for a gain resonance.

The dielectric constant $\epsilon(\omega)$ for the ensemble of the QDs can be described by the dielectric theory of Maxwell-Garnett (MG) [35, 36, 37, 38], which for two quantum dot species can be written as

$$\frac{\epsilon(\omega) - \epsilon_i(\omega)}{\epsilon(\omega) + 2\epsilon_i(\omega)} = x_1 \frac{\epsilon_{QD1}(\omega) - \epsilon_i(\omega)}{\epsilon_{QD1}(\omega) + 2\epsilon_i(\omega)} + x_2 \frac{\epsilon_{QD2}(\omega) - \epsilon_i(\omega)}{\epsilon_{QD2}(\omega) + 2\epsilon_i(\omega)} = Q, \quad (7)$$

where x_i is the volume fraction of the i -th QD species and ϵ_i is the background dielectric constant. It is assumed that the QDs are spherical and that macroscopic dielectric constants can be applied. Equation (7) provides an approximate means to account for polarization charge from a mismatch between the QD and background dielectric constant. Solving (7) for ϵ gives

$$\epsilon = \frac{\epsilon_i(1 + 2Q)}{1 - Q}. \quad (8)$$

We focus on CdSe QDs and use Equation (6) to find the QD dielectric constant, and then (7) and (8) to determine the homogenized dielectric constant for the QD mixture in a background. For CdSe, $m_e^*/m_0 = 0.1$, where m_0 is the electron rest mass, and $\epsilon_\infty = 10.2$. Also, the exciton resonance energy can be calculated for CdSe QDs with different radii. For example, $\hbar\omega_{ex} = 3.23$ eV for $R = 1.5$ nm, $\hbar\omega_{ex} = 2.55$ eV for $R = 2$ nm, and $\hbar\omega_{ex} = 1.91$ eV for $R = 4$ nm. Based on past fabrication techniques that produced CdSe QDs with linewidths of $\hbar\gamma = 0.04$ eV at room temperature and $\hbar\gamma = 0.02$ eV at 10 K, (and were limited by the variation in dimension of the QDs) [33], we optimistically assume that state of the art QD fabrication technique can reduce the linewidths to around $\hbar\gamma = 0.01$ eV, or lower.

Panel (a) of Figure 9 gives ϵ_{QD} for the CdSe QD for several $\hbar\gamma$ values. Notice that $\hbar\gamma \leq 0.02$ is necessary to achieve a negative dielectric constant. The dependency of ϵ_{QD} on R is shown in panel (b) of Figure 9. From this figure, it is evident that QDs with higher exciton energies and smaller R values offer more negative dielectric constants.

We require $\epsilon'' = 0$ at some frequency in order to achieve lossless surface plasmons and hence lossless waveguide modes. To investigate prospects for obtaining isotropic material, consider distributions of two types of QDs, one providing an absorptive resonance and the other gain. The gain resonance is assumed to be at $\hbar\omega_{ex} + \hbar\delta$, where $\hbar\omega_{ex}$ is the loss resonance and $\hbar\delta$ the difference energy achieved through a small reduction in dot size. Equal lossy and gain QD fill fractions are assumed, i.e., $x_1 = x_2$. Panel (a) of Figure 10 gives example results that indicate that a condition of $\epsilon'' = 0$ and $\epsilon' < -1$ can be achieved with moderate to high fill fractions and a sufficiently low linewidth $\hbar\gamma = 0.007$ eV. Panel (b) of Figure 10 shows a comparison between each of the plots of the effective dielectric constant in panel (a), obtained using the MG mixing rule, and the effective dielectric constant obtained via a different effective medium parameter extraction procedure. In this procedure, the effective medium parameters are extracted from a full-wave electromagnetic simulation of the transmission through a slab comprising periodic inclusions of QDs [39]. While for a low filling factor ($x_1 = x_2 = 0.1$), the effective dielectric constant values are very close to those obtained by the MG mixing rule, the effective dielectric constant

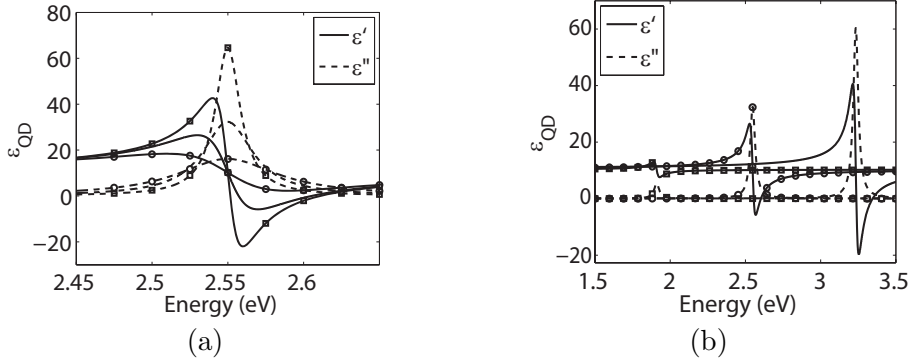


Figure 9: (a) Dielectric constant for a CdSe QD with $R = 2$ nm and $h\gamma = 0.01$ eV (squares), 0.02 eV (no symbol), and 0.04 eV (circles). (b) Dielectric constant for a CdSe QD with varying R and $h\gamma = 0.02$ eV: $R = 1.5$ nm (no symbol), $R = 2$ nm (circles), $R = 4$ nm (squares).

values for a higher filling factor ($x_1 = x_2 = 0.2$) differ, to some extent, from the corresponding MG mixing rule values. We conclude that the MG mixing rule can give a good qualitative approximation to behavior of the QD mixture, which helped in the initial prediction that the condition of $\epsilon'' = 0$ and $\epsilon' < -1$ could be met for a loss-gain QD mixture. However for future experimental pursuits, where accurate prediction of the values of ϵ' is important, a numerical effective medium parameters extraction procedure, such as the one we compared the MG results with in this work, will be required.

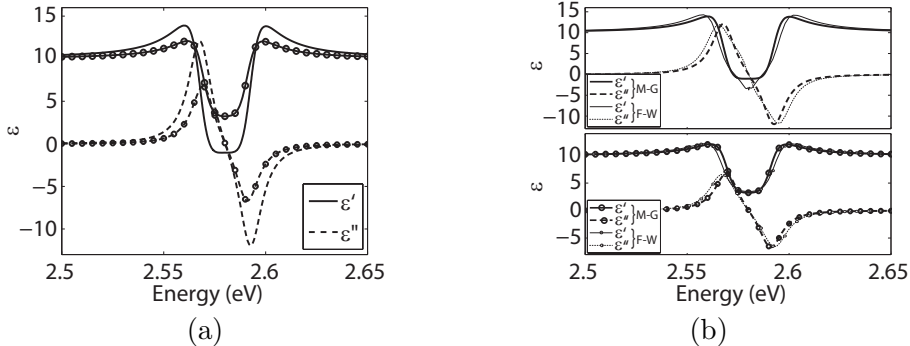


Figure 10: (a) Effective dielectric constant for $R \approx 2$ nm CdSe QDs with $\epsilon_i = 10$ and $h\delta = 0.06$ eV, with $x_1 = x_2 = 0.2$ (no symbols) and $x_1 = x_2 = 0.1$ (circles), assuming $h\gamma = 0.007$ eV. The gain is at the higher frequency. (b) Comparison of each of the plots in (a) that were obtained using Maxwell-Garnett (M-G) mixing rule, with plot obtained via a full-wave (F-W) effective medium parameter extraction procedure.

3.5 The influence of granularity in a negative refractive index lens

We demonstrate the influence of the lattice geometry or the degree of granularity on the image resolution of a negative index lens. This provides a quantitative measure of the necessary dipole density for achieving substantially subwavelength resolution. Our results thus place experimental programs to achieve enhanced resolution at optical frequencies in perspective.

A simple measure of the influence of granularity is the finite difference solution of Maxwell's equations, where a point-wise representation is used. A numerical dispersion relation can be developed for the discrete problem as [40]

$$\left(\frac{k_x}{k_0}\right)^2 \operatorname{sinc}^2\left(\pi \frac{k_x \Delta_x}{\lambda_0}\right) + \left(\frac{k_z}{k_0}\right)^2 \operatorname{sinc}^2\left(\pi \frac{k_z \Delta_z}{\lambda_0}\right) = \mu\epsilon, \quad (9)$$

where Δ_x and Δ_z are the mesh dimensions in the x - and z -directions, respectively, $\operatorname{sinc}(x) = (\sin x)/x$, μ is the relative permeability, and ϵ is the dielectric. The exact analytical dispersion relation is given by $k_{xa}^2 + k_{za}^2 = k_0^2 \mu \epsilon$. We set $k_x = k_{xa}$ and use (9) to find the $k_z = k_{za} + \delta k_z$ for the discrete problem, where δk_z is the error due to the discrete representation. Figure 11 shows the normalized discretization

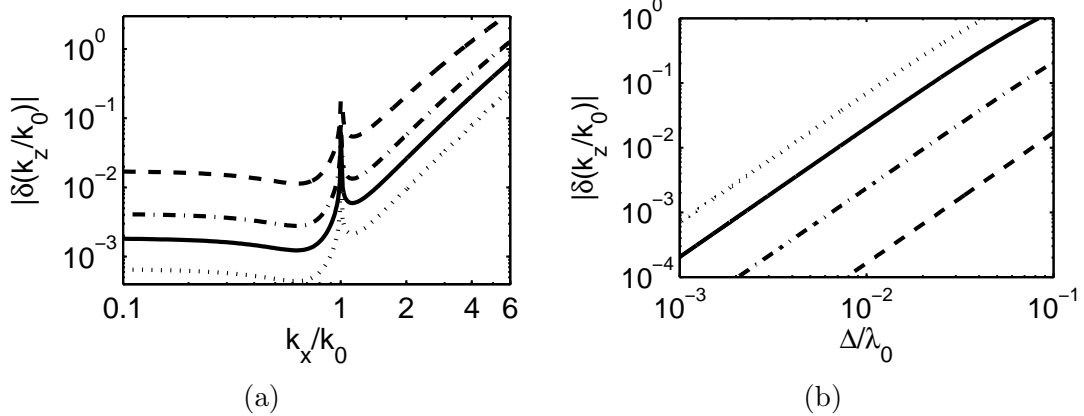


Figure 11: Numerical dispersion error for a square finite difference mesh of dimension Δ . (a) $|\delta(k_z/k_0)|$ as a function of k_x/k_0 for: $\Delta/\lambda_0 = 1/10$ (dashed line); $\Delta/\lambda_0 = 1/20$ (dash-dotted line); $\Delta/\lambda_0 = 1/30$ (solid line); $\Delta/\lambda_0 = 1/50$ (dotted line). (b) $|\delta(k_z/k_0)|$ as a function of Δ/λ_0 for: $k_x/k_0 = 0$ (dashed line); $k_x/k_0 = 2$ (dash-dotted line); $k_x/k_0 = 4$ (solid line); $k_x/k_0 = 6$ (dotted line).

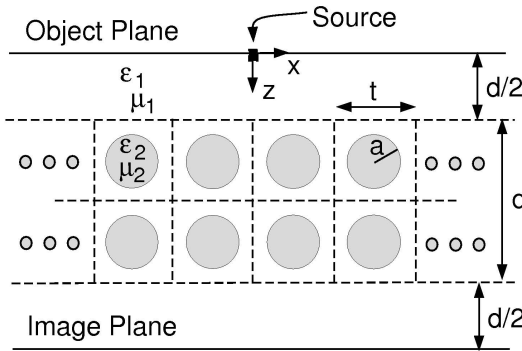


Figure 12: Discrete negative refractive index slab, where the electric and magnetic dipoles are represented by a periodic structure with material having effective $\epsilon = -1$ and $\mu = -1$.

error $|\delta(k_z/k_0)|$ as a function of k_x/k_0 and Δ/λ_0 . The fields are evanescent for $k_x/k_0 > 1$. Note that the error for the evanescent fields grows dramatically with k_x/k_0 and Δ/λ_0 . A common guideline for computational domains of a few wavelengths is that at least 20 grid points per wavelength are needed to capture the propagating field phase front. Taking $\Delta/\lambda_0 = 0.05$ in Fig. 11(b) for the $k_x/k_0 = 0$ curve, a comparable error for the $k_x/k_0 = 6$ plane wave requires $\Delta/\lambda_0 \sim 2 \times 10^{-3}$ (500 grid points per wavelength).

To understand the impact of granularity in a negative refractive index slab, we propose a model that makes for a tractable numerical problem. Figure 12 shows the model we use for a discrete metamaterial slab, where circular cylinders on a square lattice having parameters ϵ_2 and μ_2 , selected appropriately, produce homogenized parameters ϵ and μ . Each cylinder in Fig. 12 is a model for coincident electric and magnetic dipoles. We do not consider how these parameters may be achieved physically (for example, through some arrangement of conductors), only that some ϵ_2 and μ_2 give rise to $\epsilon = -1$ and $\mu = -1$. The incident field is excited in a very small region in the object plane above the slab. Varying the density of the cylinders allows us to quantitatively appraise the impact of granularity on image resolution. In our calculations we assume a TM-polarized field (\mathbf{H} parallel to the cylinders). Assigning effective medium parameters requires operation near the center of the Brillouin zone, i.e., with sufficient dipole density. We apply considerable care in forming homogenized parameters that result in a good approximation to $n = -1$, because our study requires the influence of material mismatch to be small relative to that for granularity. We should note that the periodic system of Fig. 12 has discrete Bloch modes (in k_x) at each $k_0\sqrt{\mu\epsilon}$ [41], and that we solve for the scattered fields without enforcing periodicity to capture the imaging performance.

For a TM-polarized incident wave, we determine the effective μ using $\mu = \mu_2 f + \mu_1(1 - f)$, where f is the fill fraction, i.e., the ratio of the circle to the unit cell areas in Fig. 12. The continuity of the

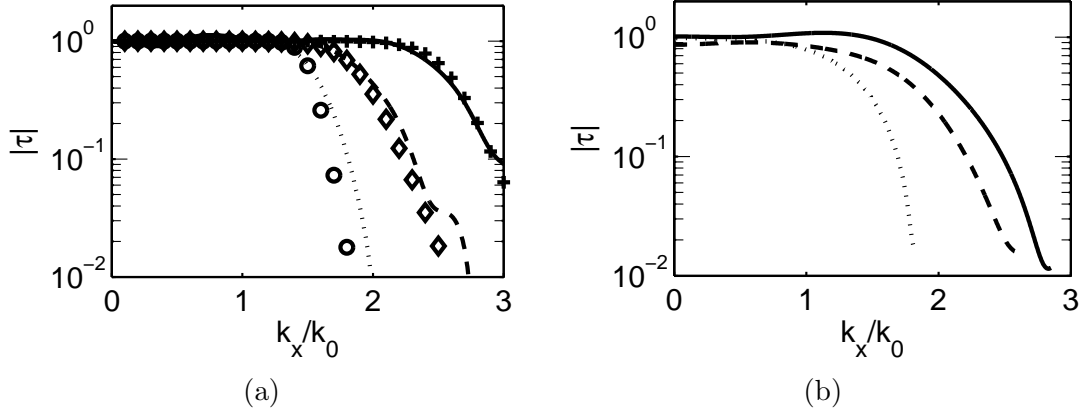


Figure 13: (a) Transfer function for a homogeneous slab lens: $d = 0.5\lambda_0$ and $\epsilon''/\epsilon' = 10^{-3}$ (solid line); $d = 0.5\lambda_0$ and $\epsilon''/\epsilon' = 10^{-2}$ (dashed line); $d = \lambda_0$ and $\epsilon''/\epsilon' = 10^{-3}$ (dotted line). The symbols are the results using the plane wave transfer function for each case. (b) The transfer function for the discrete slab lens (Fig. 12) for $d = 0.5\lambda_0$, a fill fraction of 0.5, $\epsilon_1 = 1$, $\epsilon_2 = -1.377$, $\mu_1 = 1$ and $\mu_2 = -3$: 30 cells per λ_0 (dotted line); 40 cells per λ_0 (dashed line); 50 cells per λ_0 (solid line).

magnetic field at the surface of the cylinder makes this a satisfactory choice. With fill fraction $f = 0.5$, $\mu_2 = -3$ and $\mu_1 = 1$ result in $\mu = -1$, and we assume this case. To calculate the effective ϵ , we use a numerical electrostatic model [42]. We solve Laplace's equation for the electrostatic problem of a cylindrical rod in a square cell, as in Fig. 12, under the assumption that the cell size is small relative to the optical wavelength. Considering the case with fill fraction 0.5, we choose $\epsilon_2 = -1.377$ and $\epsilon_1 = 1$ to produce $\epsilon = -1$.

A finite element method was used to solve the TM wave equation

$$\nabla \cdot (\epsilon^{-1} \nabla H_y(x, z)) + k_0^2 \mu H_y(x, z) = 0 \quad (10)$$

for the two-dimensional scattered magnetic field $H_y(x, z)$, where $k_0 = \omega/c$ is the wave number (ω is the circular frequency and c is the speed of light). The computational domain was terminated in a Sommerfeld-type radiation boundary condition. The slab width will affect the image resolution [43], as will truncation of the data set in space. We made the computation domain as large as possible and established an adequate mesh density, given the constraint on the number of unknowns presented by computer memory. In the simulation of the discrete slab, a sufficiently large discrete region (of thickness d , referring to Fig. 12) was placed between regions having continuous material. The reason for this is the granular region requires a much high finite element mesh density, and this allows a compromise to extract results of sufficient accuracy to allow conclusions on the impact of granularity. In addition, to alleviate the influence of a finite slab, we placed a radiation boundary, assuming a homogeneous slab, along the regions of the computational boundary defining the ends of the slab, making the slab appear to be (approximately) infinite in extent. The field in the image plane ($H_{yi}(x)$) and the object plane ($H_{yo}(x)$) were then Fourier transformed and the ratio formed to determine the complex transmission coefficient as a function of the transverse spatial spectral variable,

$$\tau(k_x) = \frac{H_{yi}(k_x)}{H_{yo}(k_x)}, \quad (11)$$

where $k_z = \sqrt{k_0^2 - k_x^2}$. Evaluating the performance of $\tau(k_x)$ for the evanescent fields ($k_x > k_0$) provides an important measure on possible subwavelength imaging performance.

To establish the accuracy of our numerical approach, we compare the finite element solution for a homogeneous slab lens with the exact plane wave solution [2]. Figure 13(a) shows various transfer functions for a homogeneous slab lens with assumed continuous material parameters ($\epsilon_2 = -\epsilon' + i\epsilon''$, with $\epsilon' = 1$, and $\mu_2 = -1$) and a free space background ($\epsilon_1 = 1$ and $\mu_1 = 1$), calculated using the plane wave transfer function [2] and by the finite element method, with a spatial Fourier transform of the fields in the object and image planes. Notice that we are able to capture the low-pass characteristics with the finite element solution, and that these vary, depending on the degree of loss. This data provides a reference for the potential accuracy in solving the discrete structure problem of Fig. 12. The finite

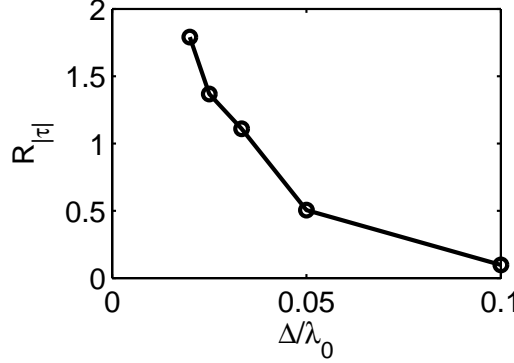


Figure 14: The resolution $R_{|\tau|}$ as a function of Δ/λ_0 for $d = 0.5\lambda_0$, a fill fraction of 0.5, $\epsilon_1 = 1$, $\epsilon_2 = -1.377$, $\mu_1 = 1$, and $\mu_2 = -3$.

element results for a discrete slab having 30, 40, and 50 cells per free space wavelength (λ_0) are given in Fig. 13(b), where effective $\epsilon = -1$ and $\mu = -1$, as determined using the homogenization procedure we have described. Increasing granularity in this range reduces the plane wave spectrum bandwidth, as does dissipative loss. It appears that the required dipole density can be viewed as a density relative to the wavelength in the transverse direction, $\lambda_x = 2\pi/k_x$. In order to maintain an adequate finite element mesh density, for an accurate solution, we were limited to a cylinder cell density of about 50 cells per λ_0 . Subwavelength resolution is related to the bandwidth of the plane wave spectrum, and it is clear from Fig. 13(b) that a very high density is needed to correctly capture a significant portion of the evanescent field spectrum. From Fig. 13(b), the $|\tau(k_x/k_0)|/\sqrt{2}$ point with 50 cells per λ_0 corresponds to $k_x/k_0 \sim 2$. The finite difference dispersion error results of Fig. 11 indicate that the error in k_z , δk_z , at this density and for $k_x/k_0 = 2$, is similar to that with a density of 20 mesh points per wavelength for the propagating waves. It thus appears that the finite difference numerical dispersion error model of (9) may indeed be a useful measure to determine the necessary level of granularity in a negative index slab. We define the resolution $R_{|\tau|} = k_{xm}/k_0$, where k_{xm}/k_0 is the value at $|\tau| = 1/\sqrt{2}$. Fig. 14 shows our calculated results for the resolution as a function of Δ/λ_0 . Appreciable evanescent field content clearly requires a very high structure density ($(\Delta/\lambda_0)^{-1}$).

The Poynting vector results for the cases of Fig. 13 provide image information. Figure 15 shows S_z , the z -component of the Poynting vector, for the homogeneous slab (Fig. 15(a)) and the discrete slab (Fig. 15(b)), normalized by the maximum of the z -component of the Poynting vector in the object plane. The image resolution improves with reducing loss and increasing dipole (cylinder) density. This finding is consistent to the results of the transfer functions shown in Fig. 13. Notice that the Poynting vector in the image plane shows negative power density regions. These are associated with vortices that we found in negative index slabs with small amount of loss [2], and they occur here because of the level of granularity.

The quantitative numerical studies of the influence of discreteness in a negative index slab lens indicate that a very high density of electric and magnetic dipoles will be necessary to achieve substantially subwavelength resolution. This may preclude the use of lithography as a means to define metallic dipoles at optical wavelengths, should subwavelength feature resolution be the goal, and suggests that alternate strategies be considered.

3.6 A perfect lens material condition from adjacent absorptive and gain resonances

Perhaps the most important property of a slab composed of a negative refractive index (or left-handed) material [4] is its ability to amplify evanescent plane waves [5], subject to loss, mismatch in the real part of the refractive index, and the dipole density [44, 1, 45]. A sufficient requirement for a negative refractive index is that the dielectric constant and the permeability be simultaneously negative. While naturally occurring negative index material is not available, conducting electric and magnetic dipoles (metamaterials) operating in the effective medium limit have been shown to exhibit a negative refractive index [46]. Of note, zero loss at the operating frequency would potentially allow perfect imaging, the prospect of which is of enormous importance in microscopy, semiconductor device processing, and optical

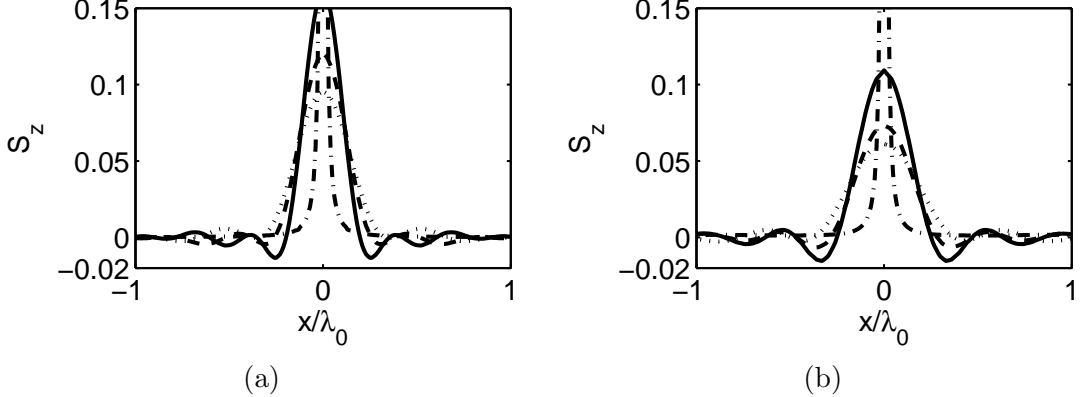


Figure 15: The z -component of the Poynting vector in the image plane normalized by the maximum z -component of the Poynting vector for the incident field. (a) Homogeneous slab (Fig. 13(a)): $d = 0.5\lambda_0$ and $\epsilon''/\epsilon' = 10^{-3}$ (solid line); $d = 0.5\lambda_0$ and $\epsilon''/\epsilon' = 10^{-2}$ (dashed line); $d = \lambda_0$ and $\epsilon''/\epsilon' = 10^{-3}$ (dotted line). (b) Discrete slab (Fig. 13(b)) with $d = 0.5\lambda_0$, a fill fraction of 0.5, $\epsilon_1 = 1$, $\epsilon_2 = -1.377$, $\mu_1 = 1$ and $\mu_2 = -3$: 30 cells per λ_0 (dotted line); 40 cells per λ_0 (dashed line); 50 cells per λ_0 (solid line). The dash-dotted lines in (a) and (b) show the z -component of the incident Poynting vector in the object plane.

memory. There has been interest in using gain to offset loss, which has led to the fundamental question as to whether it is possible to achieve a zero loss operating condition with the dielectric constant and the permeability both negative [47]. We show for a causal system described by multiple resonances that adjacent gain and loss resonances provide the possibility of achieving the material property characteristic of a perfect lens [5], and a resolution subject to the geometrical arrangement.

The Kramers-Kronig relations, which describe the spectral relationship between the real and imaginary parts of, for example, the dielectric constant, are widely used [48]. These relations form a Hilbert transform pair that results from the application of the residue theorem of Cauchy [49] in the complex $\omega = \omega' + i\omega''$ plane, and are given by

$$\begin{aligned} \zeta'(\omega) - 1 &= \frac{2}{\pi} \int_0^\infty \frac{\omega' \zeta''(\omega')}{\omega'^2 - \omega^2} d\omega' \\ \zeta''(\omega) &= \frac{-2\omega}{\pi} \int_0^\infty \frac{\zeta'(\omega') - 1}{\omega'^2 - \omega^2} d\omega', \end{aligned} \quad (12)$$

where $\zeta = \zeta' + i\zeta''$ and $\zeta = \{\mu, \epsilon, n^2\}$, with μ the permeability, ϵ the dielectric constant, and n^2 the square of the refractive index, and the integral is interpreted as a principal value, with the pole residue evaluated. The requirement for these relations to hold is that, for $\exp(-i\omega t)$, $\zeta(\omega)$ be analytic in the upper half ω plane. Satisfaction of the Kramers-Kronig relations guarantees causality, as does an analytic $\epsilon(\omega)$ in the upper half plane in complex ω space. An assumed solution to (12) leads to our claim that a perfect lens is in principle possible.

Equation (12) is based on the (electric and magnetic) response being zero before some retarded, causal time, $t_r = l/c$, where l is the distance between the source and dipole position and c is the speed of light in vacuum, regardless of the material parameters [50]. Use of group velocity in establishing the causal time, i.e., energy transport, is imprecise (because of the wave packet basis in the Fourier domain), and it is erroneous to use the phase velocity, which is opposite in direction to the Poynting vector (the direction of power flow) for a negative index material. The Kramers-Kronig relations do not convey the causal time, just that there is a local time ($t = 0$) prior to which the dipole moment is zero. They can thus be applied to any realizable system, with or without gain (stimulated emission), and with positive or negative refractive index, but not one with upper half-plane poles.

From a classical oscillator development [48] or a quantum mechanical derivation [51], the electric susceptibility can be written in the form

$$\chi(\omega) = \frac{e^2}{\epsilon_0 m} \sum_j \frac{\Delta N_j f_j}{\omega_j^2 - \omega^2 - i\gamma_j \omega}, \quad (13)$$

where e is the electron charge, ϵ_0 is the free space permittivity, m is the mass, ΔN_j is the oscillator density for the j -th resonance ($\Delta N_j > 0$ corresponds to loss and $\Delta N_j < 0$ to gain), f_j is a normalized

oscillator strength ($\sum_j f_j = 1$), and γ_j is the linewidth (γ_j^{-1} is the photon lifetime). The linewidth is broadened by inelastic collisions (with phonons) and elastic phase-destroying collisions. We consider that the electric and magnetic response (for a metamaterial operating in the effective medium limit where homogenization is appropriate) can be represented by responses of the form of (13), as can a gain mechanism. The poles of (13) occur at

$$\omega = \pm \frac{1}{2} (4\omega_j^2 - \gamma_j^2) - i\frac{\gamma_j}{2}, \quad (14)$$

where $\gamma_j > 0$ for both loss (absorption) and gain (stimulated emission). Any $\chi(\omega)$ that can be expressed in the form of (13) is both causal and analytic in the upper half of the complex ω plane.

Consider now the case of two resonances in (13), one with loss and one with gain. The fundamental question of interest is whether it is possible to have $\chi''(\omega_p) = 0$ ($\epsilon''(\omega_p) = 0$ and $\mu''(\omega_p) = 0$) at a frequency where $\chi' < -1$ (both $\epsilon'(\omega_p) < 0$ and $\mu'(\omega_p) < 0$). We write the (electric or magnetic) susceptibility as

$$\chi = \frac{a_1}{\omega_1^2 - \omega^2 - i\omega\gamma_1} + \frac{a_2}{\omega_2^2 - \omega^2 - i\omega\gamma_2}. \quad (15)$$

As a simplification, let $\gamma_1 = \gamma_2 = \gamma$, and $a_1 = -a_2 = a$, where the latter condition forces one of the resonances to offer gain. Using these parameters and solving (15) for $\chi'' = \chi_1'' + \chi_2'' = 0$ leads to

$$\omega = \omega_p = \pm \sqrt{\frac{\omega_1^2 + \omega_2^2}{2}}. \quad (16)$$

Letting $2\gamma^2 = (\omega_2 - \omega_1)^2$ gives

$$\chi'(\omega_p) = \frac{2a}{\omega_1^2 - \omega_2^2}. \quad (17)$$

In (17), $\chi'(\omega_p) < 0$ when $a > 0$ (loss at ω_1 and gain at ω_2), assuming $\omega_1 < \omega_2$.

The (electric or magnetic) susceptibility in (15) is causal and hence is a physically meaningful description of a metamaterial. As $\chi'(\omega_p)$ can be negative with the appropriate choice of parameters, it is possible to have both μ' and ϵ' negative at a frequency where both μ'' and ϵ'' are zero. Figure 16 shows the case of (15), with $\omega_1 = 0.3$ and $\omega_2 = 0.45$ (giving $\omega_p = 0.38$), and for $a = \pm\omega_1^2$. Notice that only the case for gain at the higher frequency produces negative χ' ($\chi' \sim -2$, close to the perfect lens condition for a vacuum background) and $\chi'' = 0$ at a single frequency ($\omega = \omega_p$). There is thus no fundamental reason why a metamaterial with gain cannot achieve these conditions and hence it is in concept possible to achieve the perfect lens condition for an incident field with frequency ω_p [5] and to avoid the deleterious affect of even small loss [1, 45].

The physical lens arrangement will dictate the image resolution. One suggestion has been an infinitely wide slab having $n = -1$ [5]. Any implementation must involve a finite width slab. With a gain mechanism, the reflectivity of the truncating boundaries will regulate the spontaneous emission spectrum. With a thin, wide lens, the influence of the finite width can be many orders of magnitude smaller than the impact of loss (and material mismatch) on the evanescent field components of the image [45]. Subject to the difficult task of achieving adequate gain, this paves the way to far-subwavelength imaging. Perfect imaging can be achieved with a finite width slab by placing the slab and the object within a pair of coplanar conductors, assumed perfect at this stage. The boundary conditions on these surfaces, or image theory, produces a periodic field solution in the transverse direction. With a point source, the periodic extension involves an infinite array of point sources. With $n = -1$, this infinite array is perfectly replicated at the image plane, with the appropriate slab thickness. Therefore, in this waveguide configuration, with the object field confined within the transverse spatial support of the two conductors, the object is perfectly replicated at the image plane. The efficacy of this approach depends on the influence of the finite conductivity of the conductor surfaces. Good conductors are needed only at the wavelength of operation, and control of the reflectivity at the pump wavelength may be beneficial in transverse pumping.

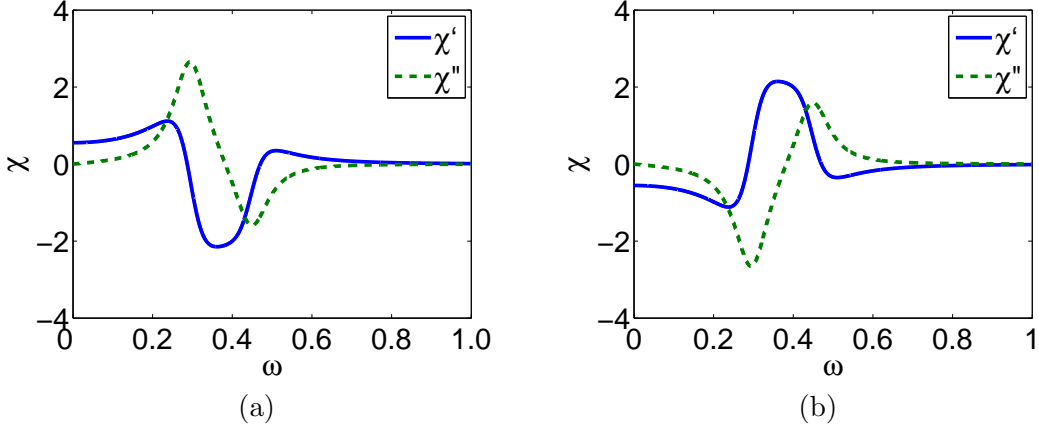


Figure 16: Susceptibilities $\chi = \chi' + \chi''$ from (15), with $\omega_1 = 0.3$ and $\omega_2 = 0.45$, for: (a) $a = \omega_1^2$, giving a loss resonance at ω_1 and gain at ω_2 , and (b) $a = -\omega_1^2$, producing gain at ω_1 and loss at ω_2 .

With loss and gain resonances, and the gain being at a higher frequency, a causal dispersion model suggests the perfect lens condition can be approached in the limit of ideal parameters: $n = -1$ and a suitable or suitably large transverse truncation. How effectively these conditions can be approached is a technology issue and, most fundamentally, this hinges on whether an adequate gain mechanism can be realized. Any artificial material must also have a satisfactorily matched real part of the refractive index and an adequate dipole density.

4 References

1. K. J. Webb, M. Yang, D. W. Ward, and K. A. Nelson, “Metrics for negative-refractive-index materials,” *Phys. Rev. E* **70**, 035602 (2004).
2. M. Yang and K. J. Webb, “Poynting vector analysis of a superlens,” *Opt. Lett.* **30**, 2382–2384 (2005).
3. K. J. Webb and M. Yang, “Subwavelength imaging with a multilayer silver film structure,” *Opt. Lett.* **31**, 2130–2132 (2006).
4. V. G. Veselago, “The electrodynamics of substances with simultaneously negative values of ϵ and μ ,” *Sov. Phys. Uspekhi* **10**, 509–514 (1968).
5. J. B. Pendry, “Negative refractive index makes a perfect lens,” *Phys. Rev. Lett.* **85**, 39663969 (2000).
6. K. J. Webb and M. Yang, “Subwavelength imaging with a multilayer silver film structure,” *Opt. Lett.* **31**, 2130–2132 (2006).
7. P. A. Belov, “Backward waves and negative refraction in uniaxial dielectrics with negative dielectric permittivity along the anisotropy axis,” *Microwave Opt. Technol. Lett.* **37**, 259–263 (2003).
8. K. J. Webb and M. Yang, “Subwavelength imaging with a multilayer silver film structure,” *Opt. Lett.* **31**, 2130–2132 (2006).
9. S. A. Ramakrishna and J. B. Pendry, “Removal of absorption and increase in resolution in a near-field lens via optical gain,” *Phys. Rev. B* **67**, 201101 (2003).
10. B. Wood, J. B. Pendry, and D. P. Tsai, “Directed subwavelength imaging using a layered metal-dielectric system,” *Phys. Rev. B* **74**, 115116 (2006).
11. P. A. Belov and C. R. Simovski, “Canalization of subwavelength images by electromagnetic crystals,” *Phys. Rev. B* **71**, 193105–193108 (2005).
12. P. A. Belov and Y. Hao, “Subwavelength imaging at optical frequencies using a transmission device formed by a periodic layered metal-dielectric structure operating in the canalization regime,” *Phys. Rev. B* **73**, 113110–113113 (2006).
13. P. A. Belov and M. G. Silveirinha, “Resolution of subwavelength transmission devices formed by a wire medium,” *Phys. Rev. E* **73**, 056607–056615 (2006).
14. N. Engheta, A. Salandrino, and A. Alù, “Circuit elements at optical frequencies: nanoinductors, nanocapacitors, and nanoresistors,” *Phys. Rev. Lett.* **95**, 095504 (2005).
15. N. Engheta, “Circuits with light at nanoscales: optical nanocircuits inspired by metamaterials,” *Science* **317**, 1698–1702 (2007).
16. E. Shamonina, V. Kalinin, K. Ringhofer, and L. Solymar, “Imaging, compression and Poynting vector streamlines for negative permittivity materials,” *Electron. Lett.* **37**, 1243–1244 (2001).
17. S. A. Ramakrishna, J. B. Pendry, M. C. K. Wiltshire, and W. J. Stewart, “Imaging the near field,” *J. Mod. Opt.* **50**, 1419–1430 (2003).
18. R. Wangberg, J. Elser, E. E. Narimanov, and V. A. Podolskiy, “Nonmagnetic nanocomposites for optical and infrared negative-refractive-index media,” *J. Opt. Soc. Am. B* **23**, 498–505 (2006).

19. D. M. Pozar, in *Mircowave Engineering*, 3rd ed. (John Wiely & Sons, Inc., 2005), pp. 412–416.
20. Y.-F. Huang *et al.*, “Improved broadband and quasi-omnidirectional anti-reflection properties with biomimetic silicon nanostructures,” *Nature Nanotech.* **2**, 770–774 (2007).
21. *Handbook of Optical Constants of Solids*, E. D. Palik, ed., (Academic Press., New York, 1998).
22. K. J. Webb and J. Li, “Analysis of transmission through small apertures in conducting films,” *Phys. Rev. B* **73**, 33401 (2006).
23. K. J. Webb and J. Li, “Resonant Slot Optical Guiding in Metallic Nanoparticle Chains,” *Phys. Rev. B* **72**, 201402R (2005).
24. K. J. Webb and J. Li, “Resonant waveguide field enhancement in dimers,” *Opt. Lett.* **31**, 3348–3350 (2006).
25. C. Delerue, G. Allan, and Y. M. Niquet, “Collective excitations in charged nanocrystals and in close-packed arrays of charged nanocrystals,” *Phys. Rev. B* **72**, 195316 (2005).
26. L. E. Brus, *J. Chem. Phys.* **80**, 4403 (1984).
27. S. Schmitt-Rink, D. A. B. Miller, and D. S. Chemla, “Theory of the linear and nonlinear optical properties of semiconductor microcrystallites,” *Phys. Rev. B* **35**, 8113–8125 (1987).
28. P. G. Bolcatto and C. R. Proetto, “Shape and dielectric mismatch effects in semiconductor quantum dots,” *Phys. Rev. B* **59**, 12487–12498 (1999).
29. A. Franceschetti, H. Fu, L. W. Wang, and A. Zunger, “Many-body psuedopotential theory of excitons in InP and CdSe quantum dots,” *Phys. Rev. B* **60**, 1819–1829 (1999).
30. Z. Yu, J. Li, D. B. O’Connor, L. Wang, and P. F. Barbara, “Large resonant Stokes shift in CdS nanocrystals,” *J. Phys. Chem. B* **107**, 5670–5674 (2003).
31. D. J. Norris, A. L. Efros, M. Rosen, and M. G. Bawendi, “Size dependence of exciton fine structure in CdSe quantum dots,” *Phys. Rev. B* **53**, 16347–16354 (1996).
32. M. Nirmal, B. O. Dabbousi, M. G. Bawendi, J. J. Macklin, J. K. Trautman, T. D. Harris, and L. E. Brus, “Fluorescence intermittency in single cadmium selenide nanocrystals,” *Nature* **383**, 802–804 (1996).
33. C. B. Murray, C. R. Kagan, and M. G. Bawendi, “Synthesis and characterization of monodisperse nanocrystals and close-packed nanocrystal assemblies,” *Annu. Rev. Mater. Sci.* **30**, 545–610 (2000).
34. X. Peng, J. Wickham, and A. P. Alivisatos, “Kinetics of II-VI and III-V colloidal semiconductor nanocrystal growth: focussing of size distributions,” *J. Am. Chem. Soc.* **120**, 5343–5344 (1998).
35. J. C. Maxwell-Garnett, “Colours in metal glasses and in metallic films,” *Philos. Trans. R. Soc. Lond.* **203**, 385–420 (1904).
36. J. C. Maxwell-Garnett, “Colours in metal glasses, in metallic films, and in metallic solutions. II,” *Philos. Trans. R. Soc. Lond.* **205**, 237–288 (1906).
37. R. W. Cohen, G. D. Cody, M. D. Coutts, and B. Abeles, “Optical properties of granular silver and gold films,” *Phys. Rev. B* **8**, 3689–3701 (1973).
38. J. I. Gittleman and B. Abeles, “Comparison of the effective medium and the Maxwell-Garnett predictions for the dielectric constants of granular metals,” *Phys. Rev. B* **15**, 3273–3275 (1977).
39. D. R. Smith, S. Schultz, P. Markoš, and C. M. Soukoulis, “Determination of effective permittivity and permeability of metamaterials from reflection and transmission coefficients,” *Phys. Rev. B* **65**, 195104 (2002).
40. S. L. Ray, “Numerical Disperion and Stability Characteristics of Time-Domain Methods on Nonorthogonal Meshes,” *IEEE Trans. Antennas Propagat.* **41**, 233–235 (1993).
41. L. Brillouin, *Wave propagation in periodic structures* (Dover, 1953).
42. V. Myroshnychenko and C. Brosseau, “Finite-element method for calculation of the effective permittivity of random inhomogeneous media,” *Phys. Rev. E* **71**, 016701 (2005).
43. L. Chen, S. He, and L. Shen, “Finite-Size Effects of a Left-Handed Material Slab on the Image Quality,” *Phys. Rev. Lett.* **92**, 107404 (2004).
44. D. R. Smith, D. Schurig, M. Rosenbluth, S. Schultz, S. A. Ramakrishna, and J. B. Pendry, “Limitations on sub-diffraction imaging with a negative refractive index slab,” *Appl. Phys. Lett.* **82**, 1056 (2003).
45. M. Yang and K. J. Webb, “Poynting vector analysis of a superlens,” *Opt. Lett.* **30**, 2382–2384 (2005).
46. R. A. Shelby, D. R. Smith, and S. Schultz, “Experimental verification of a negative index of refraction,” *Science* **292**, 77–79 (2001).
47. M. Stockman, “Criterion for negative refraction with low optical losses from a fundamental principle of causality,” *Phys. Rev. Lett.* **98**, 177404 (2007).
48. J. D. Jackson, *Classical Electrodynamics*, 3 ed. (Wiley, New York, NY, 1999).
49. E. C. Titchmarsh, *Introduction to the Theory of Fourier Integrals* (Oxford University Press, Oxford, UK, 1948).
50. L. Brillouin, *Wave Propagation and Group Velocity* (Academic Press, New York, NY, 1960).
51. A. Yariv, *Quantum Electronics*, 2 ed. (Wiley, New York, 1975).